



# *In-situ* $\text{Li}_7\text{La}_3\text{Zr}_2\text{O}_{12}/\text{LiCoO}_2$ interface modification for advanced all-solid-state battery



Takehisa Kato<sup>a,d</sup>, Tadashi Hamanaka<sup>b</sup>, Kazuo Yamamoto<sup>b</sup>, Tsukasa Hirayama<sup>b</sup>, Fumihiro Sagane<sup>c</sup>, Munekazu Motoyama<sup>a,d</sup>, Yasutoshi Iriyama<sup>a,d,\*</sup>

<sup>a</sup> Department of Materials, Physics and Energy Engineering, Graduate School of Engineering, Nagoya University, Furo-cho, Chikusa-ku, Nagoya 464-8603, Japan

<sup>b</sup> Japan Fine Ceramics Center, 2-4-1 Mutsuno, Atsuta-ku, Nagoya 456-8587, Japan

<sup>c</sup> Department of Materials Science and Chemical Engineering, Faculty of Engineering, Shizuoka University, 3-5-1 Johoku, Naka-ku, Hamamatsu, Shizuoka 432-8561, Japan

<sup>d</sup> JST-ALCA, 5, Sanbancho, Chiyoda-ku, Tokyo 102-0075, Japan

## H I G H L I G H T S

- Nb layer is introduced to LLZ/LiCoO<sub>2</sub> interface in all-solid-state battery.
- Nb-based-interface modification decreases the interfacial resistivity.
- LLZ/LiCoO<sub>2</sub> interface modification improves cycle stability and rate capability.

## A R T I C L E I N F O

### Article history:

Received 6 January 2014

Received in revised form

24 February 2014

Accepted 27 February 2014

Available online 20 March 2014

### Keywords:

All-solid-state-lithium batteries

LLZ

Niobium

Interface modification

Interfacial resistivity

## A B S T R A C T

The inherent high resistance of electrolyte/electrode interface in all-solid-state-lithium-secondary batteries (SSLB) poses a significant hurdle for the SSLB development. The interfacial resistivity between  $\text{Li}_7\text{La}_3\text{Zr}_2\text{O}_{12}$  (LLZ) and  $\text{LiCoO}_2$  is decreased by introducing a thin Nb layer ( $\sim 10$  nm) at this interface. The interface modification approach using a Nb interlayer dramatically improves the discharge capacity and rate capability of a SSLB.

© 2014 Elsevier B.V. All rights reserved.

## 1. Introduction

Improving the safety and energy density of lithium-ion batteries (LIBs) have been important goals for power source applications of large-scale devices such as electric vehicles. Hence, the development of all-solid-state-lithium-secondary batteries (SSLBs) with incombustible inorganic solid electrolytes is highly anticipated. There are two challenges in developing SSLBs to achieve comparable performance to those of commercial LIBs with organic liquid electrolytes: (i) increasing lithium-ion ( $\text{Li}^+$ ) conductivity of solid electrolyte and (ii) decreasing large interfacial resistance between the electrode and the electrolyte. Among the various kinds of solid

electrolytes [1–3], oxide-based-solid electrolytes are safe and chemically stable because of their lower reactivity with gaseous components in the air. In particular, garnet-structured  $\text{Li}_7\text{La}_3\text{Zr}_2\text{O}_{12}$  (LLZ) discovered by Murugan et al. has received much attention due to its chemical stability with Li metal in addition to a wide potential window and a relatively high  $\text{Li}^+$  conductivity ( $5 \times 10^{-4} \text{ S cm}^{-1}$ ) [4]. Extensive studies on improving the  $\text{Li}^+$  conductivity of LLZ have been subsequently conducted [5–7]. Of these, LLZ where Zr is partially exchanged with Nb has an even greater conductivity of  $8 \times 10^{-4} \text{ S cm}^{-1}$  than the original LLZ [8].

However, when a common positive electrode,  $\text{LiCoO}_2$ , is combined with LLZ, mutual diffusions of Co and La, Zr between  $\text{LiCoO}_2$  and LLZ occurs at the interface during a thermal treatment when depositing thin  $\text{LiCoO}_2$  films on LLZ pellets [9]. Generally, oxide-based-solid electrolytes are physically inflexible, and as such the

\* Corresponding author. Tel./fax: +81 52 789 3235.

E-mail address: [iriama@numse.nagoya-u.ac.jp](mailto:iriama@numse.nagoya-u.ac.jp) (Y. Iriyama).

battery fabrication process requires an additional heating step to improve adhesion between the electrode and the electrolyte. The mutual diffusion region where  $\text{LiCoO}_2$  and LLZ intermix can play a role in assisting a strong bonding between electrode and electrolyte, but instead the resulting mutual diffusion layer becomes a significant resistor at the interface. Problems regarding this mutual diffusion have been reported in several studies of SSLBs, especially when sulfide solid electrolytes are combined with electrode active materials such as  $\text{LiCoO}_2$ . In those cases, electrolyte/electrode interface modification has been suggested as an effective method to reduce interfacial resistivity [10–12]. Also, amorphous materials are often used to stabilize interfacial reactions and reduce the resistivity between solid electrolyte and electrode [13–15]. In fact, thin film batteries using lithium phosphorus oxynitride glass electrolyte show fast charge–discharge reactions for over a few thousands of cycles [15]. Hence, the idea of *in-situ* forming amorphous layer in the electrolyte/electrode interface has attracted our interest. In this methodology, a  $\text{Li}^+$ -conductive-amorphous material is produced at the interface through spontaneous reactions triggered by heating between an electrode and an electrolyte.

This work shows a new strategy of interface modification for a SSLB. A thermal treatment following deposition of a Nb metal layer onto LLZ produces a low-resistivity-amorphous layer. As a result, the interfacial resistivity decreases from  $2600 \Omega \text{ cm}^2$  to  $150 \Omega \text{ cm}^2$  depending on the thickness of the Nb metal layer. The resultant amorphous materials are characterized by transmission electron microscopy (TEM), energy dispersive X-ray (EDX) analyses, and nano-diffraction methods.

## 2. Experimental

### 2.1. Preparation of Li/LLZ/LiCoO<sub>2</sub> batteries

Mirror-polished-dense pellets (12 mm in diameter, 1–2 mm in thickness) of garnet-structured LLZ were fabricated by following the procedure in previous work [5]. A thin Nb metal layer was deposited on one side of each LLZ pellet by radio frequency (RF) magnetron sputtering in an Ar atmosphere at room temperature. After Nb deposition, a sample was annealed at 873 K for 2 h in an  $\text{O}_2$  atmosphere. This procedure helps Nb and LLZ regions intermix into each other and more tightly bond at their interfaces. A  $\text{LiCoO}_2$  film with a thickness of 150 nm was deposited on the Nb-modified surface by pulsed laser deposition (PLD) at 873 K for 1.5 h using a lithium-rich-sintered-Li-Co-O-pellet target ( $\text{Li/Co} = 1.40$ ) [20]. During the PLD, a fourth-harmonic Nd:YAG laser ( $\lambda = 266 \text{ nm}$ ) was focused on a pellet with an energy fluence of  $0.85 \text{ J cm}^{-2}$  and a repetition frequency of 10 Hz.  $\text{O}_2$  gas was introduced into the chamber to maintain its pressure at 27 Pa during the deposition. The target-to-substrate distance was 46.5 mm. A thin film of Pt was coated on a PLD-grown- $\text{LiCoO}_2$  film by RF magnetron sputtering. Subsequently, a sample was transported into an Ar-filled-glove box. A Li negative electrode was deposited by vacuum evaporation on the opposite side of an LLZ pellet to the side with  $\text{LiCoO}_2$ . After deposition of a thin Li film, a sample was heated at 453 K for 1 h while being pressed with a spring-loaded-disk clamp. The geometric electrode area of a finished SSLB cell ( $\text{Li/LLZ/LiCoO}_2$ ) was  $0.64 \text{ cm}^2$ .

### 2.2. Electrochemical measurements of Li/LLZ/LiCoO<sub>2</sub> batteries

Electrochemical measurements of our cells were performed by CV and AC impedance analyses. CV measurements were carried out between 3.2 V and 4.2 V with a potential sweep rate of  $0.1 \text{ mV s}^{-1}$ . The interfacial resistance of LLZ/LiCoO<sub>2</sub> interfaces was determined by AC impedance spectroscopy. The resistances for LLZ bulk and Li/LLZ interfaces were estimated using a symmetric blocking electrode

cell ( $\text{Pt/LLZ/Pt}$ ) and a symmetric non-blocking electrode cell ( $\text{Li/LLZ/Li}$ ), respectively. Pt films of a blocking cell and Li films of a non-blocking cell were deposited on the two sides of LLZ pellets by RF magnetron sputtering and vacuum evaporation, respectively. A non-blocking cell was heated while being appropriately pressed with a disk clamp as conducted when a SSLB cell was fabricated. The geometric electrode areas of these cells were  $0.64 \text{ cm}^2$ . AC impedance spectra from a sample were recorded by applying sine waves of voltage with amplitude of 14 mV in the frequency range from 200 kHz to 1 Hz. All the electrochemical measurements were conducted in an Ar-filled-glove box at room temperature. Cell performances of fabricated SSLBs were characterized by constant-current-constant-voltage measurements. Charge current was set at  $1 \text{ mA cm}^{-2}$ . Discharge current was initially  $1 \text{ mA cm}^{-2}$ , which sequentially changed to 2, 5, 10,  $1 \text{ mA cm}^{-2}$  after every five cycles. The cutoff voltage in a charging process was set to be 4.2 V. After the voltage reached 4.2 V, the recording mode instantly switched to a constant voltage measurement retaining the voltage as 4.2 V. The current was recorded until it dropped below  $1 \text{ mA cm}^{-2}$ . Then, it turned to a discharging mode. The cutoff voltage for a discharge was 3.2 V. Once the discharge voltage became 3.2 V with a certain current density, a current transient was recorded while retaining the voltage at 3.2 V until it dropped below  $1 \text{ mA cm}^{-2}$ .

### 2.3. Characterization methods of Li/LLZ/LiCoO<sub>2</sub> batteries

Crystal microstructures near LLZ/LiCoO<sub>2</sub> interfaces were characterized by TEM. LLZ samples for TEM analyses were prepared by the focused ion beam (FIB) technique. However, LLZ quickly suffers catastrophic damage in  $\text{Ga}^+$  beams. Hence, we developed the special pre-coating technique for LLZ samples with conductive and protective layers. Eventually, TEM observations including nanobeam diffractions and EDX analyses were successfully conducted for LLZ even though the resulting thicknesses of observed regions were more than 150 nm. This may be part of the reason that the electron diffraction patterns are blurred as presented in the following section. Elemental mapping in the vicinity of LLZ/LiCoO<sub>2</sub> interfaces was conducted by STEM equipped with an EDX spectrometer. XRD ( $\text{CuK}\alpha$  source, Rigaku Ultima IV) analyses were conducted for mixed powders of LLZ and Nb after heated at 873 K under an  $\text{O}_2$  flow for 2 h. Diffraction spectra were collected in the  $2\theta$  range from  $10^\circ$  to  $60^\circ$  at a scan rate of  $1^\circ \text{ min}^{-1}$ .

## 3. Results & discussion

### 3.1. Electrochemical measurements

Fig. 1(a) shows cyclic voltammograms (CVs) of Li/electrolyte/LiCoO<sub>2</sub> samples with  $1.0 \text{ mol dm}^{-3} \text{ LiClO}_4$  in propylene carbonate (solid line) and LLZ (broken line) electrolytes. Large redox peaks are observed at a redox potential of 3.9 V in a liquid electrolyte due to  $\text{Li}^+$  insertion/extraction reactions with  $\text{LiCoO}_2$ . Two couples of smaller redox peaks appear at 4.05 V and 4.15 V. They represent  $\text{LiCoO}_2$  crystal phase transitions from the hexagonal to monoclinic (HM) and monoclinic to hexagonal (MH') crystal phases [16]. On the other hand, the electrode reaction rates in a solid-electrolyte cell are significantly smaller than in a liquid-electrolyte cell because the redox peak profiles are totally blunted and exhibit an asymmetric shape in a solid-electrolyte cell. Similar results were also reported in previous work [9].

Fig. 1(b) shows CVs of solid-electrolyte cells with Nb modification layers introduced at the LLZ/LiCoO<sub>2</sub> interfaces. The thicknesses of Nb layers vary from 7 to 15 nm. The broken lines in Fig. 1(a) and (b) are identical. The reaction rates for  $\text{Li}^+$  insertion/extraction reactions in voltage sweeping are clearly improved in Nb-modified

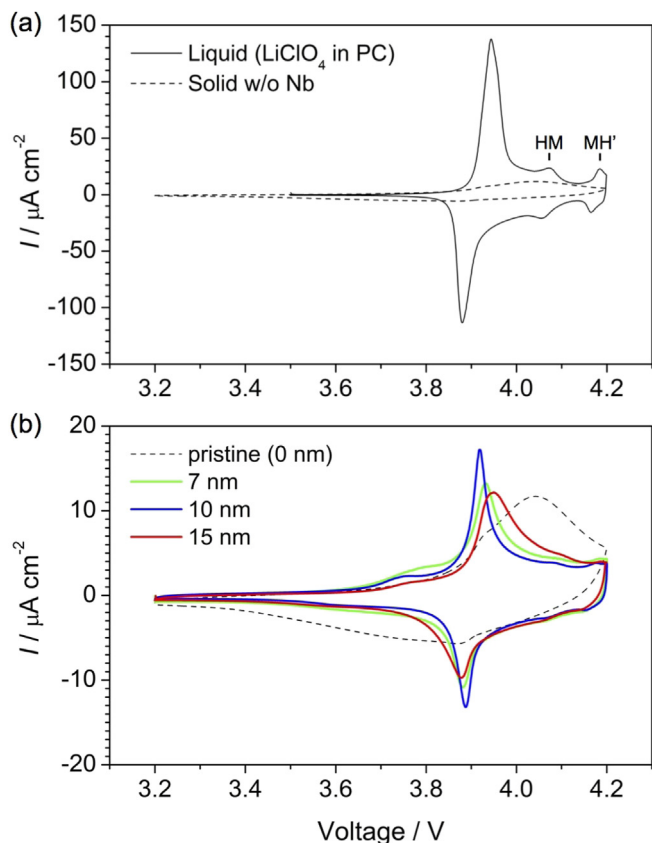


**Fig. 1.** (a) CVs for Li/electrolyte/LiCoO<sub>2</sub> batteries with (solid line) LiClO<sub>4</sub> in propylene carbonate and (dashed line) LLZ electrolytes. (b) CVs for Li/LLZ/LiCoO<sub>2</sub> batteries with and without Nb-modifications. The thicknesses of Nb layers between LLZ and LiCoO<sub>2</sub> are (black) 0, (green) 7, (blue) 10, and (red) 15 nm. Scan rate = 0.1 mV s<sup>-1</sup>. (For interpretation of the references to color in this figure legend, the reader is referred to the web version of this article.)

cells. The LiCoO<sub>2</sub> crystal phase transitions between hexagonal and monoclinic crystal phases with smaller redox peaks are even observed near 4.05 V and 4.15 V as seen with a liquid electrolyte in Fig. 1(a). The substrate temperatures for depositing thin LiCoO<sub>2</sub> films by PLD (873 K) are maintained constant. The presence of Nb modification layers at LLZ/LiCoO<sub>2</sub> interfaces drastically changes the shapes of CVs in Fig. 1(b).

Fig. 2(a) and (b) shows Nyquist plots obtained from alternating current (AC) impedance spectroscopy measurements for non-

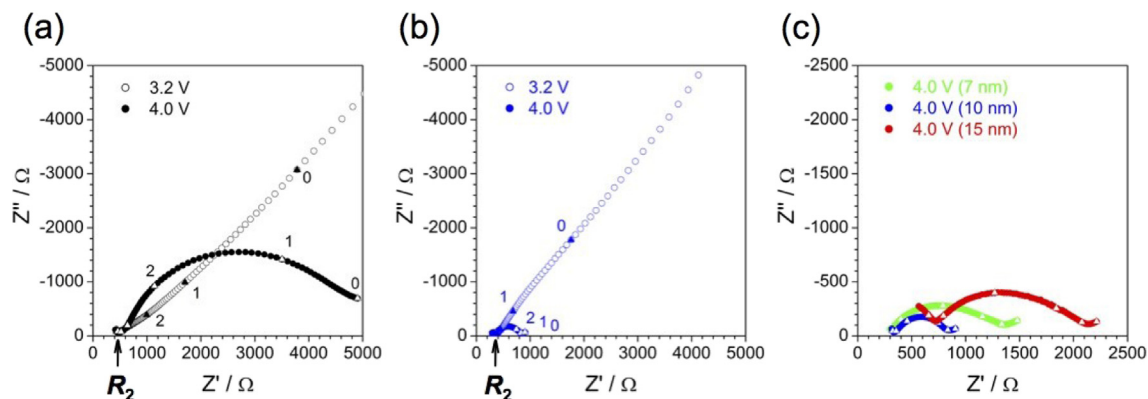
modified and Nb-modified LLZ cells sandwiched with Li and LiCoO<sub>2</sub> electrodes, respectively. The Nb modification layer thickness is 10 nm in Fig. 2(b). The AC impedance measurements were carried out at 3.2 V, which equals the lowest limit of the sweep range in Fig. 1(b), and at 4.0 V.

The Nyquist plots obtained at 3.2 V draw straight diagonal lines in Fig. 2(a) and (b). The intercepts of these straight lines with the real axes indicate the DC resistance values of LLZ pellets. The grain boundary resistances of LLZ pellets have usually been observed in frequency ranges on the order of 10<sup>4</sup> Hz [4,5]. The frequency values of the plots near the straight-line onsets on the real axes are 10<sup>4</sup> Hz. The direct current (DC) resistance of an LLZ pellet and the charge transfer resistance for Li/LLZ interface ( $R_1$ ) were estimated using a symmetric blocking cell (Pt/LLZ/Pt) and a non-blocking cell (Li/LLZ/Li), respectively. The DC resistance of an LLZ pellet ranges from approximately 0.5–1.0 kΩ depending on the pellet thickness [Figure S1(a) and (b) in the Supporting information]. The  $R_1$  was 170 Ω cm<sup>2</sup>, and its characteristic frequency is in the range of 10<sup>4</sup>–10<sup>3</sup> Hz. Hence, the higher frequency end of a diagonal line indicates the total resistance of LLZ ( $R_2$ ) including bulk and grain boundaries.

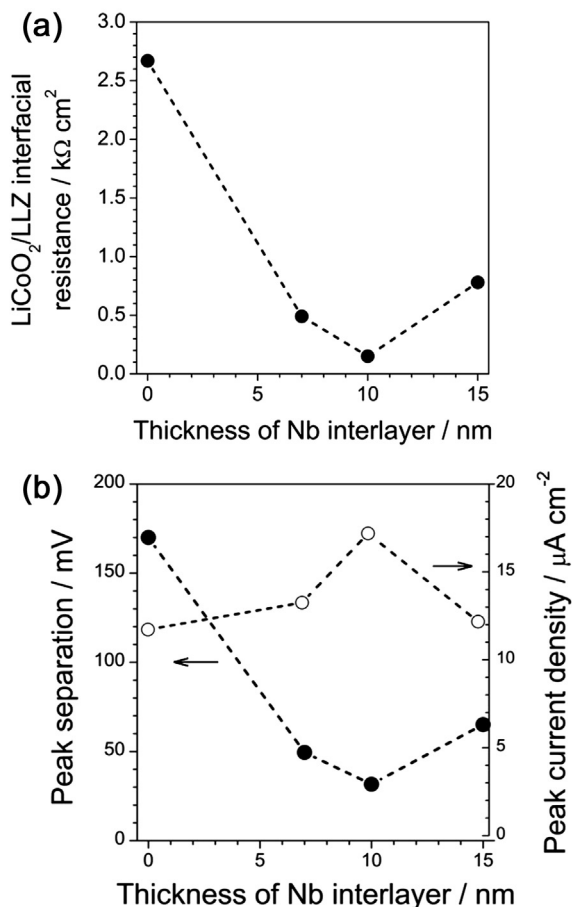
At 4.0 V, the straight lines disappear, and semicircular arcs appear in the low frequency range from 10<sup>4</sup> to 10<sup>1</sup> Hz in Fig. 2(a) and (b). These arcs are attributed to the electrochemical reactions through interfaces of Li and LiCoO<sub>2</sub> with LLZ. The charge transfer resistance of non-modified or Nb-modified LLZ/LiCoO<sub>2</sub> interface ( $R_3$ ) can thus be obtained by subtracting  $R_1$  from the diameter of a larger arc appearing at 4.0 V in the low frequency range.

Fig. 2(c) shows AC impedance spectra at 4.0 V from Nb-modified Li/LLZ/LiCoO<sub>2</sub> cells with 7, 10, 15-nm-thick Nb layers. The higher and lower frequency ends on the real axes of the semicircular arcs observed in Fig. 2(c) correspond to  $R_2$  and  $R_1 + R_2 + R_3$ , respectively. There are sample-to-sample variations in LLZ pellet thickness, whereby  $R_2$  is not perfectly constant. The overall charge transfer resistance (i.e.,  $R_1 + R_3$ ) varies depending on the Nb layer thickness as seen in Fig. 2(c).  $R_1$  is expected to be constant. Thus, it is found that  $R_3$ , which is the charge transfer resistance for Nb-modified LLZ/LiCoO<sub>2</sub> interface, is a function of Nb layer thickness.

The resistivity of LLZ/LiCoO<sub>2</sub> interfaces as a function of Nb layer thickness is shown in Fig. 3(a). A non-modified cell has a  $R_3$  of 2600 Ω cm<sup>2</sup>. On the other hand, Nb interface modification decreases  $R_3$  by one order of magnitude. The smallest resistivity of 150 Ω cm<sup>2</sup> is obtained with a 10-nm-thick-Nb layer. This result suggests that there is an optimum range for a Nb layer thickness for minimizing the interfacial resistivity. Fig. 3(b) shows the peak separations and peak current densities in CVs in Fig. 1(b) as function of Nb layer thickness. The peak separation and peak current density become the minimum and maximum, respectively, when



**Fig. 2.** Nyquist plots for Li/LLZ/LiCoO<sub>2</sub> batteries. (a) 0-nm Nb at 3.2 V and 4.0 V, (b) 10-nm Nb at 3.2 V and 4.0 V, (c) 7, 10, 15-nm Nb at 4.0 V. The meaning of  $R_1$  is explained in Subsection 3.1.  $n$ : data points measured at 10<sup>n</sup> Hz.



**Fig. 3.** The effects of Nb layer thickness on (a) LLZ/LiCoO<sub>2</sub> interfacial resistances at 4.0 V and (b) peak separations and peak current densities in the CVs in Fig. 1(b).

the  $R_3$  is the smallest in Fig. 3(a). Hence, the shapes of the CV curves in Fig. 1(b) are clearly dominated by the LLZ/LiCoO<sub>2</sub> interfacial resistances.

On the other hand, Ta is considered to also be an attractive candidate for an interface modification material. This is because Ta-exchanged LLZ is a solid electrolyte with a high Li<sup>+</sup> conductivity [17]. Also, amorphous Li–Ta–O is a Li<sup>+</sup>-conductive material [18]. Therefore we hence tested the effect of Ta as an interlayer as well, and found that a Ta modification also decreases the interfacial resistivity. The lowest interfacial resistivity with Ta was measured to be 500 Ω cm<sup>2</sup>. Hence, Nb is more effective to remedy highly resistive LLZ/LiCoO<sub>2</sub> interfaces.

### 3.2. TEM observations

Fig. 4(a) shows a scanning-TEM (STEM) image in the high-angle-annular-dark-field (HAADF) mode of a cross-section for an LLZ/LiCoO<sub>2</sub> interface with a 10-nm-thick-Nb layer. Fig. 4(b) shows an EDX line profile from LiCoO<sub>2</sub> to LLZ regions measured in the area enclosed with the dashed lines in Fig. 4(a) where elemental mapping analyses for Co (red), Nb (purple), and La (green) were carried out.

There are two regions on the right and left sides from the central position with the largest Nb concentration in Fig. 4(b). In the region I (right side), the Co concentration is quite low while the La concentration does not significantly decrease from that in bulk LLZ. On the other hand, with increasing distance from the interface, the Zr and Nb concentrations increase and decrease respectively. It is thus

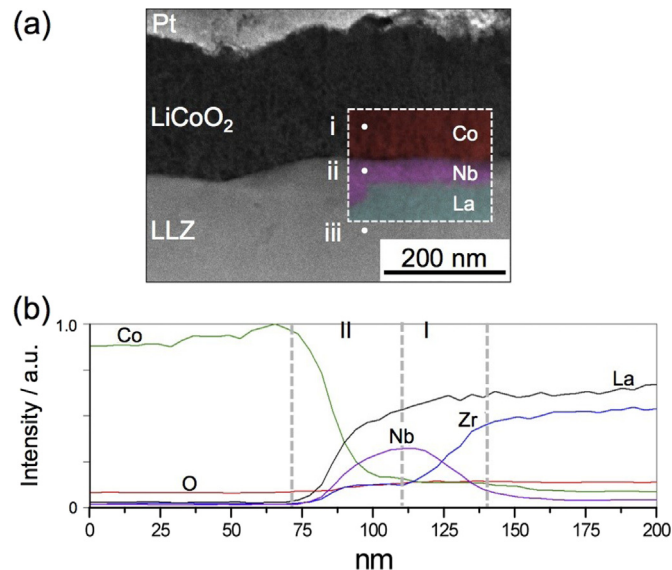


**Fig. 4.** (a) Cross-sectional-HAADF-STEM image of a Nb-modified interface between LLZ and LiCoO<sub>2</sub>. EDX elemental mappings for Co (red), Nb (purple), and La (green) are overlaid in the dashed-line-enclosed region. The top Pt is a protective layer for FIB processes. (b) EDX line profile traversing the center of the dashed-line-enclosed region in (a) from the top to the bottom (corresponding to the left-to-right direction in the graph). (For interpretation of the references to color in this figure legend, the reader is referred to the web version of this article.)

conceivable that Zr in LLZ is gradually exchanged with Nb in the region I through chemical replacement reactions.

Zr and Nb are tetravalent and pentavalent, respectively. Therefore, Li atoms diffuse out of LLZ to the Nb layer to maintain the electroneutrality. It is thus considered that Nb metal changes to Li–Nb–O compounds in the interfacial region during annealing at 873 K in O<sub>2</sub>. It is well known that Nb can dissolve in LLZ replacing Zr, resulting in sufficiently high Li<sup>+</sup> conductivity [8]. Amorphous Li–Nb–O is a Li<sup>+</sup>-conductive material with a Li<sup>+</sup>-conductivity of approximately  $1 \times 10^{-6}$  S cm<sup>-1</sup> [18]. Ohta et al. also reported small resistivity (170 Ω cm<sup>2</sup>) for the interfaces between LiCoO<sub>2</sub> and LLZ–Nb in which Zr of LLZ is partially exchanged with Nb [19].

In the region II (left side), the concentrations of La and Nb decrease while that of Co increases with distance from the interface. In our previous work, we demonstrated mutual diffusion between LiCoO<sub>2</sub> and LLZ occurs across a distance of approximately 100 nm. Eventually, the crystalline La<sub>2</sub>CoO<sub>4</sub> phase is produced [9]. On the other hand, the thickness of the mutual diffusion region (region II) in Fig. 4(b) is only 40 nm. Hence, the interface modification in the present scheme decreases the mutual diffusion length from 100 nm to 40 nm.

Fig. 5(a) shows a selected-area-electron-diffraction pattern from an area across the LLZ–Nb/LiCoO<sub>2</sub> interface. The presence of LLZ and LiCoO<sub>2</sub> is recognized in the diffraction pattern in Fig. 5(a). Nano-diffraction patterns from the locations of i, ii, and iii in Fig. 4(a) are analyzed in Fig. 5(b). Several spots are seen in the diffraction patterns from i (LiCoO<sub>2</sub>) and iii (LLZ), indicating that these regions are in crystalline phases. However, neither diffraction spots nor Debye–Scherrer rings are observed from ii where its location is between LiCoO<sub>2</sub> and LLZ, and Nb is dominantly detected by EDX. Only a hollow pattern is evident in ii. This result suggests that this interfacial region is amorphous. In XRD spectra from mixed powders of LLZ and Nb after annealing at 873 K (Figure S2 in the Supporting information), different compounds (LiNb<sub>3</sub>O<sub>8</sub>, LiNbO<sub>3</sub>) are seen slightly. Hence, we hypothesized that the amorphous interfacial region observed between LLZ and LiCoO<sub>2</sub> in



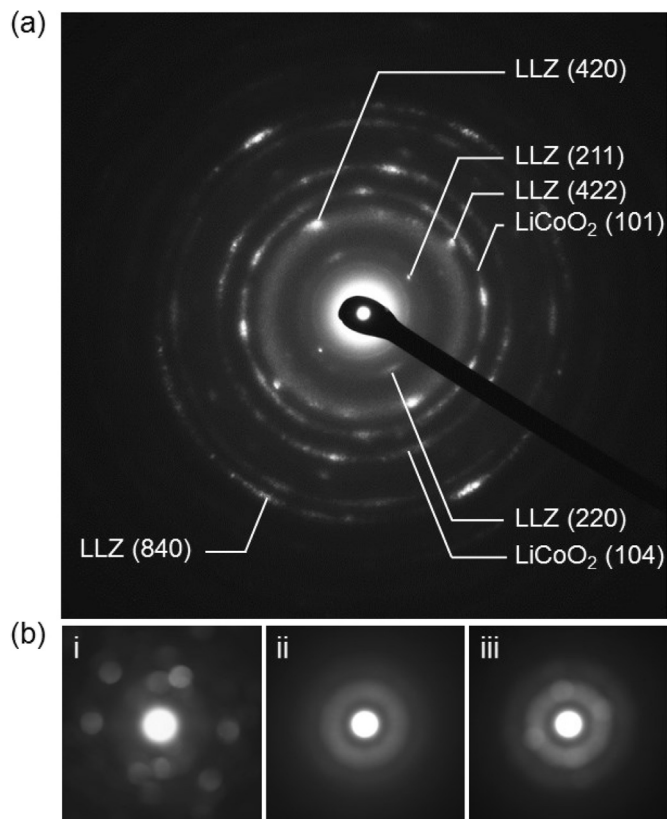


**Fig. 5.** (a) Electron diffraction pattern obtained from the image in Fig. 4(a). (b) Nano-diffraction images obtained from spots of i, ii, and iii in Fig. 4(a).

Fig. 4(a) is mostly consisting of amorphous-state  $\text{LiNbO}_3$  and  $\text{LiNb}_3\text{O}_8$ .

In Fig. 3(a), a 10-nm-thick Nb layer exhibits the smallest charge transfer resistance. Too small of an amount of deposited Nb leads to an insufficient coverage on LLZ surfaces to suppress the growth of mutual diffusion layer. On the other hand, too large of an amount of a Nb layer increases the overall resistance because an amorphous Li–Nb–O layer is essentially more resistive than LLZ. This trade-off

is the reason that an optimum range exists for this interface modification as presented in Fig. 3(a).

We also tested the interfacial resistivity at  $\text{LiCoO}_2/\text{LLZ}$  interfaces with a non-annealed-PLD interlayer fabricated from a composite target with  $\text{Nb}_2\text{O}_5$  and  $\text{ZrO}_2$  having a Nb:Zr ratio of 7:3. This value is close to the molar ratio of Nb to Zr in the center of the interface in Fig. 4(b). However, its interfacial resistivity was eventually as large as on the order of  $10^4 \Omega \text{ cm}^2$ . We hence consider that atomic diffusions of Zr and Nb to replace each other across the region I as seen in Fig. 4(b) play a critical role in creating low-resistive bonding between Li–Nb–O and LLZ layers.

Fig. 6 shows schematic illustrations of how a thin Nb layer modifies  $\text{LLZ}/\text{LiCoO}_2$  interfaces. Without a Nb layer between  $\text{LiCoO}_2$  and LLZ, they thermally react to produce partially-crystalline compounds such as  $\text{La}_2\text{CoO}_4$  with no  $\text{Li}^+$  conductivity at their interfaces during  $\text{LiCoO}_2$ –PLD at 873 K. On the other hand, a Nb layer introduced between  $\text{LiCoO}_2$  and LLZ produces a  $\text{Li}^+$ -conductive amorphous phase at their interface. The Li–Nb–O amorphous layer plays three mixed roles in lowering the interfacial resistivity, as follows. (i) The presence of Nb suppresses the extension of the mutual diffusion of non- $\text{Li}^+$ -conductive phase (e.g.,  $\text{La}_2\text{CoO}_4$ ). (ii) Voids or cavities at the atomistic scale created due to the joining of two differing crystals (i.e., LLZ and  $\text{LiCoO}_2$ ) can be eliminated by amorphous materials are inserted. The impedance spectra do not show a clear difference in electrolyte resistance between non-modified and Nb-modified SSLBs, whereas the charge transfer resistances significantly differ in Fig. 2(a) and (b). This is possibly because voids or cavities existing at  $\text{LLZ}/\text{LiCoO}_2$  interfaces in a non-modified cell are removed by Nb modification. (iii) Moreover, such amorphous materials (i.e., oxides composed of Li and Nb) have enough high values of  $\text{Li}^+$  conductivity, whereby  $\text{Li}^+$  ions can easily move across the interfaces. These functions can similarly be applied to Ta-based interface modification, which is mentioned above.

### 3.3. Cell performance

Fig. 7(a) and (b) shows charge–discharge curves of fabricated SSLBs ( $\text{Li}/\text{LLZ}/\text{LiCoO}_2$ ) with a Nb modification layer of 0 and 10 nm in thickness, respectively. The charge current density is always  $1 \text{ mA cm}^{-2}$ , whereas the discharge current density sequentially increases from  $1 \text{ mA cm}^{-2}$  to 2 and  $5 \text{ mA cm}^{-2}$  after every five cycles. In the first cycle with a discharge current density of

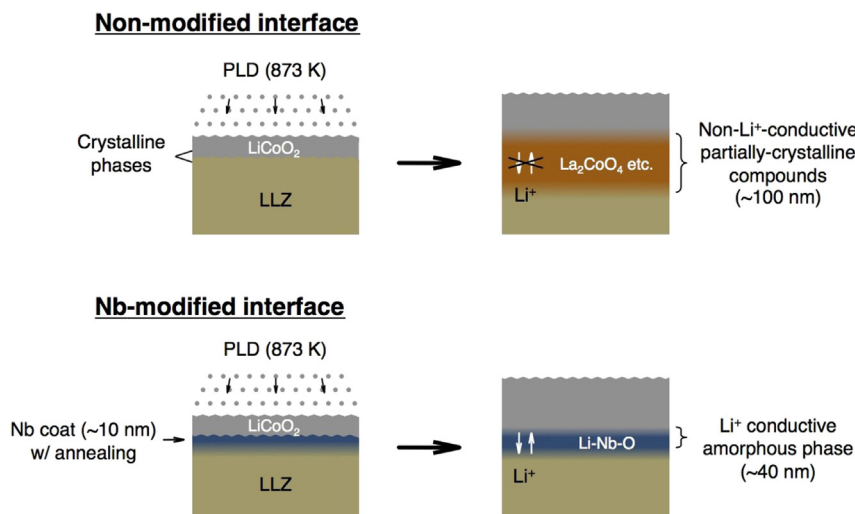


**Fig. 6.** Schematic illustrations of non-modified and Nb-modified  $\text{LLZ}/\text{LiCoO}_2$  interfaces. The mutual diffusion between LLZ and  $\text{LiCoO}_2$  produces non- $\text{Li}^+$ -conductive phases such as a crystalline  $\text{La}_2\text{CoO}_4$  phase. Nb-modified  $\text{LLZ}/\text{LiCoO}_2$  interface suppresses the mutual diffusion and produce  $\text{Li}^+$ -conductive amorphous phase.

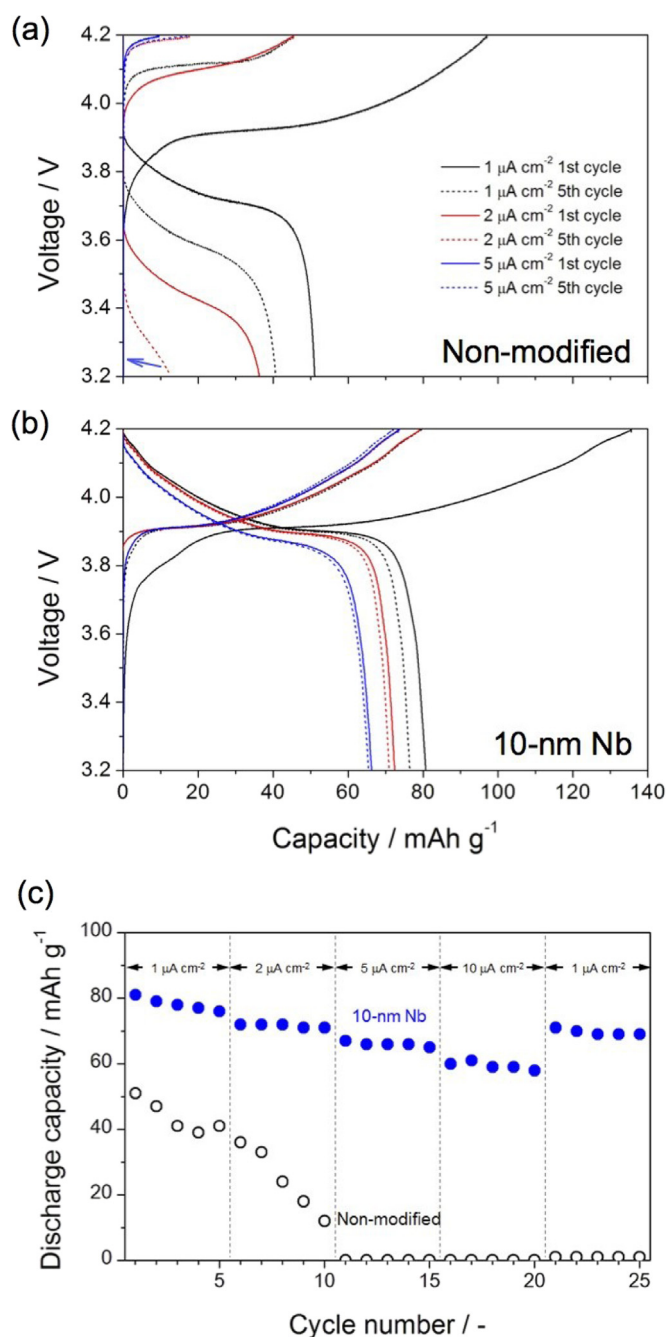


**Fig. 7.** Charge–discharge curves of Li/LLZ/LiCoO<sub>2</sub> with a Nb modification layer of (a) 0 and (b) 10 nm in thickness. These graphs display only the first and fifth cycles for each discharge current density. The arrow indicates the discharge curves at 5 mA cm<sup>-2</sup>. (c) Discharge capacity variations of non-modified and Nb-modified SSLBs with the number of charge–discharge cycles.

1 mA cm<sup>-2</sup>, the specific charge capacity of a thin LiCoO<sub>2</sub> film is approximately 100 mAh g<sup>-1</sup> with a non-modified SSLB. The following specific discharge capacity is 50 mAh g<sup>-1</sup> with a plateau voltage of approximately 3.7 V. It actually soon degrades as the cycle number increases. Additionally, as the cycle number increases, gaps between charge and discharge plateau voltages gradually increase. With a larger discharge current density of 2 mA cm<sup>-2</sup>, the capacity decreases even faster. The voltage readily drops to 3.2 V at 5 mA cm<sup>-2</sup> for a discharge [too rapid of a drop to be shown in Fig. 7(b)]. On the other hand, the specific charge capacity achieves almost 140 mAh g<sup>-1</sup> by a 10-nm-thick-Nb modification in

the first cycle with a specific discharge current density of 1 mA cm<sup>-2</sup>. The following specific discharge capacity becomes 80 mAh g<sup>-1</sup> with a plateau voltage of approximately 3.9 V. However, the specific discharge capacities and plateau voltages only slightly decrease with the cycle number in contrast to the results with a non-modified SSLB. Fig. 7(c) shows specific discharge capacity variations of SSLBs over 20 charge–discharge cycles. This result is recorded by sequentially changing discharge current density from 1 mA cm<sup>-2</sup> to 2, 5, 10, 1 mA cm<sup>-2</sup> after every five cycles. The specific discharge capacity of a non-modified SSLB sharply decreases with the cycle number. The rapid decrease is significant when the discharge current density becomes larger than 2 mA cm<sup>-2</sup>. In contrast, a Nb-modified SSLB retains its specific discharge capacity at 60 mAh g<sup>-1</sup> even for 10 mA cm<sup>-2</sup>, although it slightly decreases with discharge current density.

#### 4. Conclusions

In conclusion, we have successfully demonstrated the interface modification of introducing a thin Nb layer between LLZ and LiCoO<sub>2</sub> for a SSLB. The interfacial resistivity at LLZ/LiCoO<sub>2</sub> is decreased by one order of magnitude. TEM and EDX analyses have clarified that the Nb modification suppresses the growth of mutual diffusion layer. Also, the produced material perhaps includes an amorphous Li–Nb–O, which has been reported to be Li<sup>+</sup> conductive. Due to the formation of such amorphous material through an *in-situ* process, Nb-modified SSLBs have shown sharp redox peaks of LiCoO<sub>2</sub> with peak separations of a few tens of mV in CVs for Li<sup>+</sup> insertion/extraction reactions as observed with an organic liquid electrolyte. Moreover, this interface modification has successfully improved the cycle stability and rate capability of charge–discharge reactions of a Li/LLZ/LiCoO<sub>2</sub> solid state battery. Ta interlayers can also decrease the interfacial resistivity, albeit less effective than Nb. This interface modification strategy is thus general and can be extended to the *in-situ* formation of several Li<sup>+</sup>-conductive compounds.

#### Acknowledgment

The authors thank JST-ALCA and in part NEDO-RISING for the financial supports.

#### Appendix A. Supplementary data

Supplementary data related to this article can be found at <http://dx.doi.org/10.1016/j.jpowsour.2014.02.102>.

#### References

- [1] H. Aono, E. Sugimoto, Y. Sadaoka, N. Imanaka, G.Y. Adachi, J. Electrochem. Soc. 136 (1989) 590–591.
- [2] J.B. Bates, N.J. Dudney, G.R. Gruzalski, R.A. Zuh, A. Choudhury, C.F. Luck, J.D. Robert-son, Solid State Ionics 53 (1992) 647–654.
- [3] J. Fu, J. Am. Ceram. Soc. 80 (1997) 1901–1903.
- [4] R. Murugan, V. Thangadurai, W. Weppner, Angew. Chem. Int. Ed. 46 (2007) 7778–7781.
- [5] S. Kumazaki, Y. Iriyama, K.H. Kim, R. Murugan, K. Tanabe, K. Yamamoto, T. Hirayama, Z. Ogumi, Electrochem. Commun. 13 (2011) 509–512.
- [6] R. Murugan, S. Ramakumar, N. Janani, Electrochem. Commun. 13 (2011) 1373–1375.
- [7] J. Wolfenstine, J. Sakamoto, J.L. Allen, J. Mater. Sci. 47 (2012) 4428–4431.
- [8] S. Ohta, T. Kobayashi, T. Asaoka, J. Power Sources 196 (2011) 3342–3345.
- [9] K.H. Kim, Y. Iriyama, K. Yamamoto, S. Kumazaki, T. Asaka, K. Tanabe, C.A.J. Fisher, T. Hirayama, R. Murugan, Z. Ogumi, J. Power Sources 196 (2011) 764–767.
- [10] N. Ohta, K. Takada, I. Sakaguchi, L.Q. Zhang, R.Z. Ma, K. Fukuda, M. Osada, T. Sasaki, Electrochem. Commun. 9 (2007) 1486–1490.
- [11] A. Sakuda, A. Hayashi, M. Tatsumisago, Chem. Mater. 22 (2010) 949–956.
- [12] N. Kamaya, K. Homma, Y. Yamakawa, M. Hirayama, R. Kanno, M. Yonemura, T. Kamiyama, Y. Kato, S. Hama, K. Kawamoto, A. Mitsui, Nat. Mater. 10 (2011) 682–686.

- [13] J.B. Bates, N.J. Dudney, B. Neudecker, A. Ueda, C.D. Evans, *Solid State Ionics* 135 (2000) 33–45.
- [14] K. Kishida, N. Wada, Y. Yamaguchi, H. Inui, M. Demura, Y. Iriyama, Z. Ogumi, *J. Mater. Res.* 25 (2010) 1583.
- [15] A. Sakuda, H. Kitaura, A. Hayashi, M. Tatsumisago, Y. Hosoda, T. Nagakane, A. Sakamoto, *Chem. Lett.* 41 (2012) 260–261.
- [16] J.N. Reimers, J.R. Dahn, *J. Electrochem. Soc.* 139 (1992) 2091–2097.
- [17] H. Buschmann, S. Berendts, B. Mogwitz, J. Janek, J. Power Sources 206 (2012) 236–244.
- [18] A.M. Glass, K. Nassau, T.J. Negran, *J. Appl. Phys.* 49 (1978) 4808–4811.
- [19] S. Ohta, T. Kobayashi, J. Seki, T. Asaoka, *J. Power Sources* 202 (2012) 332–335.
- [20] Y. Iriyama, H. Kurita, I. Yamada, T. Abe, Z. Ogumia, *J. Power Sources* 137 (2004) 111–116.